JACS
JOURNAL OF THE AMERICAN CHEMICAL SOCIETY
Article
pubs.acs.org/JACS

Critical Factors Driving the High Volumetric Uptake of Methane in $Cu_3(btc)_2$

Zeric Hulvey,[*,†,‡] Bess Vlaisavljevich,[§] Jarad A. Mason,[∥] Ehud Tsivion,[∥,⊥] Timothy P. Dougherty,[†,▽] Eric D. Bloch,[∥] Martin Head-Gordon,[∥,#] Berend Smit,[§,⊗] Jeffrey R. Long,[∥,⊥] and Craig M. Brown[*,†,¶]

[†]Center for Neutron Research, National Institute of Standards and Technology, Gaithersburg, Maryland 20899, United States
[‡]Department of Materials Science and Engineering, University of Maryland, College Park, Maryland 20742, United States
[§]Department of Chemical and Biomolecular Engineering and [∥]Department of Chemistry, University of California, Berkeley, California 94720, United States
[⊥]Materials Science Division and [#]Chemical Sciences Division, Lawrence Berkeley National Laboratory, Berkeley, California 94720, United States
[▽]Department of Chemistry, Georgetown University, Washington, D.C. 20057, United States
[⊗]Institut des Sciences et Ingénierie Chimiques, Ecole Polytechnique Fédérale de Lausanne (EPFL), Lausanne, Switzerland
[¶]Department of Chemical and Biomolecular Engineering, University of Delaware, Newark, Delaware 19716, United States

Supporting Information

ABSTRACT: A thorough experimental and computational study has been carried out to elucidate the mechanistic reasons for the high volumetric uptake of methane in the metal−organic framework $Cu_3(btc)_2$ (btc^{3-} = 1,3,5-benzenetricarboxylate; HKUST-1). Methane adsorption data measured at several temperatures for $Cu_3(btc)_2$, and its isostructural analogue $Cr_3(btc)_2$, show that there is little difference in volumetric adsorption capacity when the metal center is changed. In situ neutron powder diffraction data obtained for both materials were used to locate four CD_4 adsorption sites that fill sequentially. This data unequivocally shows that primary adsorption sites around, and within, the small octahedral cage in the structure are favored over the exposed Cu^{2+} or Cr^{2+} cations. These results are supported by an exhaustive parallel computational study, and contradict results recently reported using a time-resolved diffraction structure envelope (TRDSE) method. Moreover, the computational study reveals that strong methane binding at the open metal sites is largely due to methane−methane interactions with adjacent molecules adsorbed at the primary sites instead of an electronic interaction with the metal center. Simulated methane adsorption isotherms for $Cu_3(btc)_2$ are shown to exhibit excellent agreement with experimental isotherms, allowing for additional simulations that show that modifications to the metal center, ligand, or even tuning the overall binding enthalpy would not improve the working capacity for methane storage over that measured for $Cu_3(btc)_2$ itself.

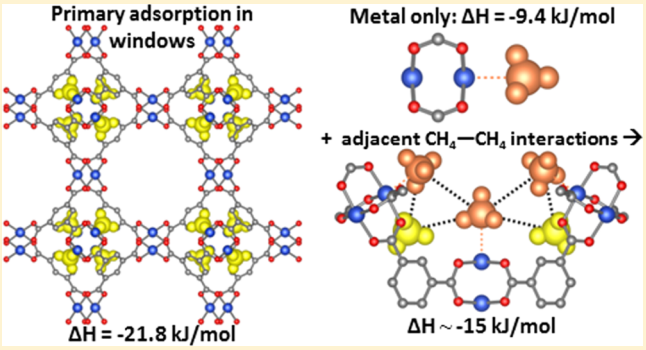

INTRODUCTION

A variety of economic and environmental factors have sparked interest in the use of natural gas, composed primarily of methane (CH_4), as an alternative transportation fuel to petroleum.[1−4] Its use in on-board vehicular applications is severely limited by its relatively low volumetric energy density. While this can be increased by compression or liquefaction, the resulting systems contain expensive, bulky, and energy-intensive components, and their usage is mainly limited to larger vehicles such as buses. The development of adsorption-based systems where high surface area materials store large volumes of CH_4 at ambient conditions would allow for the use of smaller, lightweight tanks that could be integrated into smaller vehicles such as passenger cars.[5] Metal−organic frameworks (MOFs) have attracted substantial attention as materials for these types of adsorption applications due to their high surface areas and chemically tunable pore dimensions and surface functionality.[6]

Adsorption of CH_4 in MOFs has been investigated across several structural parameters both experimentally and computationally.[7−9] It has been shown through multiple adsorption studies that $Cu_3(btc)_2$ (btc^{3-} = 1,3,5-benzenetricarboxylate; HKUST-1)[10] exhibits one of the highest volumetric capacities for CH_4 in a MOF at 35 bar and 25 °C.[7,8] Its structure consists of binuclear copper(II) paddlewheel units connected through the carboxylate linkers to form a three-dimensional pore

Received: July 2, 2015
Published: August 11, 2015

DOI: 10.1021/jacs.5b06657
J. Am. Chem. Soc. 2015, 137, 10816−10825

structure. An axial water molecule on each Cu^{2+} ion can be removed to leave an open coordination site that can attract different gas molecules. The pore structure contains three distinct types of cavities. The surface of the first of the two large pores is composed mostly of benzene rings from the linker molecules and has a diameter of ~11 Å. It is connected to a slightly larger cavity with a diameter of almost 13 Å, which contains the open Cu^{2+} sites exposed to its surface. The octahedral cage (diameter ~5 Å) is accessible through triangular windows from the largest pore. An isostructural Cr analogue can be synthesized that displays a slightly higher surface area and interesting adsorption behavior for gases such as H_2, O_2, and CO_2, but has yet to be investigated for CH_4 uptake.[11−13]

The correlation of structural features with adsorption behavior is a critical part of the evaluation of adsorptive materials and must be accomplished using a variety of experimental techniques. Powder diffraction experiments have been used to determine binding sites for many gas molecules in MOFs,[14−20] including CH_4 in $Cu_3(btc)_2$.[21−23] These studies have determined that CH_4 adsorption occurs in both the octahedral cages and at the open metal sites; however, the data in these reports did not clearly identify the relative affinity, or order of filling, of these sites. In designing improved adsorbents for CH_4 storage, it is important to have a complete understanding of the reasons for the record high volumetric storage densities of CH_4 in $Cu_3(btc)_2$. It is of particular interest to determine whether the CH_4 molecule prefers a perfectly sized cage to enhance adsorbate−adsorbent contacts or an enhanced electronic interaction at an open metal coordination site, or if these structural characteristics are of relatively equal importance. Furthermore, any differences found in the adsorptive behavior of $Cu_3(btc)_2$ and $Cr_3(btc)_2$ would reveal information regarding the nature of the CH_4−open metal site interaction. These are important details, because other gases have been shown to differ in which site they prefer in this structure. We have shown previously that noble gases within $Cu_3(btc)_2$ bind initially in the octahedral cages, and upon increased loading do not bind at all at the open metal sites.[24] The initial binding site for H_2 is at the Cu atoms in $Cu_3(btc)_2$, but at the windows to the octahedral cages in $Cr_3(btc)_2$.[12,25,26] Adsorption at the metal site is strongly preferred for O_2 in $Cr_3(btc)_2$.[11] It is clear that site preference can vary both from gas to gas and also from $Cu_3(btc)_2$ to $Cr_3(btc)_2$, and a more detailed analysis of CH_4 adsorption in these materials is necessary.

Parallel to thermodynamic and structural measurements, computational studies on adsorption in MOFs can assist in explaining experimental observations and build on experimental data to predict adsorptive behavior in other materials. These theoretical studies have become an extremely important tool to guide synthetic efforts into the design of porous materials, as once adsorptive behavior can be adequately predicted entire libraries of thousands of possible structures can be screened for their properties to expose beneficial structural features.[27−32] When studying MOFs with computational tools, multiple levels of theory are often required to properly describe guest adsorption. Through density functional theory studies, the structure and relative energetics of CH_4 binding sites can be explored. In the case studied here, higher level multiconfigurational methods allow for the electronic structure of the strong Cr−Cr bond in $Cr_3(btc)_2$ to be studied in detail. Furthermore, molecular simulations allow for the prediction of adsorption isotherms. This can be particularly challenging for materials like $Cu_3(btc)_2$ and $Cr_3(btc)_2$ that contain strong binding sites and care must be taken to ensure the guest-framework interactions are treated appropriately.

In this report, we present a comprehensive study into the mechanisms governing CH_4 adsorption in $Cu_3(btc)_2$ and $Cr_3(btc)_2$. Volumetric uptake data are presented for the first time for $Cr_3(btc)_2$, which compare closely to previous data measured for $Cu_3(btc)_2$. A detailed structural study is presented that clarifies that CH_4 binds at the windows to the octahedral cages for both materials before binding at the metal sites. Finally, several computational strategies are described that provide additional insight into the nature of the CH_4−framework interactions, as well as predict uptake behavior in some structural variations of $Cu_3(btc)_2$ and $Cr_3(btc)_2$. Analyzing all of these results concurrently leads to the conclusion that although the open metal site acts as a strong binding site for CH_4, its strength arises more from interactions with the previously adsorbed molecules at the primary site than from interactions with the metal cation itself.

EXPERIMENTAL SECTION

High-Pressure Gas Adsorption Measurements. The synthesis and activation of $Cu_3(btc)_2$ and $Cr_3(btc)_2$ were adapted from previous reports.[11,33] The successful synthesis and activation of the framework was confirmed by comparing the X-ray powder diffraction pattern and Langmuir surface area to those previously reported.

High-pressure adsorption isotherms in the range of 0 to 100 bar were measured on a HPVA-II-100 from Particulate Systems, a Micromeritics company. In a typical measurement, between 0.3 and 0.7 g of activated sample was loaded into a tared 2 mL stainless steel sample holder inside a glovebox under a N_2 atmosphere. Prior to connecting the sample holder to the Swagelok VCR fittings of the complete high-pressure assembly inside the glovebox, the sample holder was weighed to determine the sample mass.

The fully assembled sample holder was transferred to an ASAP 2020 low-pressure adsorption instrument, fitted with an isothermal jacket, and evacuated at the material's original activation temperature for at least 1 h. Then, a 77 K N_2 adsorption isotherm was measured. This was used to verify that the high-pressure sample mass was correct and that the sample was still of high quality by comparing the resulting Langmuir surface area to the expected value. Note that a specially designed OCR adapter was used to connect the stainless steel high-pressure adsorption cell directly to the ASAP 2020 analysis port.

The sample holder was then transferred to the HPVA-II-100, connected to the instrument's analysis port via an OCR fitting, and evacuated at room temperature for at least 1 h. The sample holder was placed inside an aluminum recirculating dewar connected to a Julabo FP89-HL isothermal bath filled with Julabo Thermal C2 fluid, for which the temperature stability is ±0.02 °C. A detailed description of the procedure used for measuring high-pressure CH_4 adsorption isotherms on the HPVA-II-100 was recently reported.[7] Further details regarding isotherm fitting, plots of isotherms at all temperatures, and parameters for heat of adsorption determinations are provided in the Supporting Information.

Neutron Powder Diffraction. Neutron powder diffraction (NPD) experiments were carried out on 3.3962 g of activated $Cu_3(btc)_2$ and 1.0335 g of activated $Cr_3(btc)_2$ samples using the high-resolution neutron powder diffractometer BT-1 at the National Institute of Standards and Technology Center for Neutron Research (NCNR). The samples were placed in a helium glovebox and loaded into vanadium sample cells equipped with a valve for gas loading and sealed using an indium O-ring. Data were collected using a Ge(311) monochromator with an in-pile 60′ collimator corresponding to a wavelength of 2.078 Å. The samples were loaded onto bottom-loading closed-cycle refrigerators and initial data was collected on the activated samples at 8 K. An additional pattern was measured for $Cr_3(btc)_2$ at

DOI: 10.1021/jacs.5b06657
J. Am. Chem. Soc. 2015, 137, 10816−10825

room temperature. The samples were connected through the gas loading valve to a manifold of known volume and exposed to quantitative doses of CD_4 corresponding to 0.4, 0.7, 1.5, and 2.2 CD_4 molecules per Cu atom for $Cu_3(btc)_2$, and 0.7, 1.5, and 2.2 CD_4 molecules per Cr atom for $Cr_3(btc)_2$. Deuterated methane was used in these experiments owing to the large incoherent scattering cross section of hydrogen, which would result in significantly increased background in the data. Gas was dosed at 150 K, and the sample was slowly cooled to approximately 90 K during adsorption to allow the sample to reach equilibrium. Following complete adsorption of the dose, as evidenced by a zero pressure reading inside the system, samples were then cooled to 8 K for NPD measurements. A second set of measurements at higher temperatures was carried out on the same $Cu_3(btc)_2$ sample by collecting data at 150 K following the complete adsorption of a dose of approximately 1.3 CD_4 molecules per Cu atom. The system was then heated to 295 K while open to the dosing manifold, resulting in a significant amount of desorption, as expected based on the experimental isotherm data. The sample cell and manifold equilibrated at ~1.7 bar at 295 K, corresponding to a loading level of near 0.15 CD_4 molecules per Cu atom. A 295 K data set was collected following this equilibration step.

NPD patterns were analyzed using Rietveld analysis as implemented in EXPGUI/GSAS.[34,35] The starting model for CD_4 loaded $Cu_3(btc)_2$ was taken from our previous data of the bare framework,[24] and for CD_4 loaded $Cr_3(btc)_2$ from a refined NPD pattern collected for the bare material at 8 K. Fourier difference methods were employed to locate the adsorbed CD_4 molecules.[36] Rietveld refinements of the models had the bond lengths and angles of the CD_4 molecules constrained to chemically reasonable values, and both the fractional occupancy and isotropic displacement parameter values of the five atoms in the molecule were constrained to be identical. All refined atomic parameters for all structures are included in the Supporting Information, along with final Rietveld plots and selected Fourier difference maps.

COMPUTATIONAL DETAILS

Periodic Density Functional Theory. Periodic density functional theory (DFT) calculations were performed as implemented in the VASP software package.[37] In order to treat CH_4 adsorption accurately, noncovalent interactions must be properly accounted for. The Rutgers−Chalmers van der Waals density functionals make use of a nonlocal formulation of the correlation part of the exchange-correlation energy functional and have been developed to treat both medium and long-range interactions.[38] Specifically, the dispersion-corrected vdW-DF2+U functional was employed in all calculations.[39] The Hubbard U is a parameter for metal d electrons determined to reproduce oxidation energies.[40] In this work the value was 3.8 and 3.5 eV for Cu and Cr, respectively, based on work by Wang and Ceder on metal oxides.[41] The PAW pseudopotentials were used in all calculations.[42] A plane wave basis set was employed with a cutoff of 1000 eV to compute electronic energies and the integration over the irreducible Brillouin zone was carried out over the Γ point. Atomic positions and lattice constants for the empty framework were optimized with forces converged to 10^{-7} Å/eV. Methane binding energies and enthalpies were computed using a rigid MOF approximation. Both bound and unbound CH_4 atomic positions were optimized at the same level of theory as the framework. Furthermore, harmonic vibrational frequencies were computed for the guest and used to include zero point energy and thermal corrections to the electronic energy yielding binding enthalpies.

In the periodic DFT calculations, the absolute magnetization for the ground state is 0.6 μ_B per Cu center and 0.9 μ_B per Cr center. In the case of $Cu_3(btc)_2$, the coupling between the two Cu centers in the paddlewheel is antiferromagnetic. While Cu^{2+} is d^9 and the spin state of copper paddlewheel complexes like $Cu_3(btc)_2$ is well-established, the electronic structure of $Cr_3(btc)_2$ is more challenging. Cr−Cr multiple bonds are notoriously multireference in character; therefore, cluster calculations were performed to determine the ground state. Nevertheless, in the periodic DFT calculations, three states were studied. First, the closed shell singlet (e.g., no unpaired electrons per metal center) was considered. Additionally, a magnetic ordering with 1 μ_B and 2 μ_B for each metal center was explored for the empty framework. The lowest energy state, as mentioned above, has an absolute magnetization of 0.9 μ_B per Cr center and yielded the optimized geometry with a Cr−Cr distance in best agreement with experiment. Therefore, all binding energy calculations were performed for this state, although we wish to emphasize that the ground state of $Cr_3(btc)_2$ is multiconfigurational and diamagnetic. The details of the electronic structure of the Cr−Cr bond will be discussed in detail below.

Grand Canonical Monte Carlo. Grand Canonical Monte Carlo (GCMC) simulations were performed to compute CH_4 adsorption isotherms. Framework atoms are often treated in the literature with off-the-shelf force fields like the Universal Force Field (UFF) employing mixing rules to describe the guest-framework interactions.[43] However, in cases like $Cu_3(btc)_2$, UFF dramatically underestimates binding. Recently, Kim et al.[44] noted that while the UFF force field captures adsorption behavior for most systems reasonably well, it often fails if the binding is strong. Therefore, they introduced a simple correction to ensure that the UFF force field correctly predicts the binding energy, if this binding energy is known, either from experiments or from ab initio calculations (in this case periodic DFT).[44] Simulations employing this approach are referred to as UFF-shifted in this work. The trial force field employed is UFF for the framework−CH_4 interactions and TraPPE for CH_4−CH_4 interactions.[45] Lorentz−Berthelot mixing rules were employed. The minimum binding energy is required as a parameter for both the force field to which the correction is being applied and at the higher level. In this case, the minimum binding energy with the UFF force field for $Cu_3(btc)_2$ and $Cr_3(btc)_2$ is 22.9 and 22.2 kJ/mol, respectively. Likewise, the binding energy at the vdW-DF2 level of theory is 25.4 and 24.7 kJ/mol for $Cu_3(btc)_2$ and $Cr_3(btc)_2$, respectively.

RESULTS AND DISCUSSION

Gas Adsorption Data. Gas adsorption experiments were carried out on activated samples of $Cu_3(btc)_2$ and $Cr_3(btc)_2$. Surface areas of both materials were initially measured to ensure complete activation of the materials. As expected due to its slightly larger unit cell and lower mass, $Cr_3(btc)_2$ was found to have a slightly higher Langmuir surface area (2337 m^2/g vs 2190 m^2/g), and pore volume (0.82 cm^3/g vs 0.77 cm^3/g) compared to $Cu_3(btc)_2$. High pressure CH_4 adsorption data were measured on an activated sample of $Cr_3(btc)_2$ at several temperatures from −25 to 50 °C. Adsorption data obtained using identical methods and conditions for $Cu_3(btc)_2$ were previously reported[7] and are used in this work where appropriate for comparisons to $Cr_3(btc)_2$ experimental and simulated data. The measured excess adsorption data were converted to total adsorption and fit with a single-site Langmuir equation. Using a dual-site Langmuir model did not significantly improve the overall quality of the fit, and it appears that the adsorption data are well-modeled with a single adsorption site over the entire temperature and pressure range studied in this work.

Total volumetric adsorption isotherms measured at 25 °C (Figure 1) show that $Cr_3(btc)_2$ has a slightly lower volumetric CH_4 uptake than $Cu_3(btc)_2$ at all pressures. Still, the 203 v/v of CH_4 adsorbed at 35 bar and 25 °C is one of the highest capacities ever reported for a metal−organic framework under these conditions. Since a single-site model was used to fit the isotherms, the isosteric heats of adsorption derived from these data do not vary as a function of loading. The resulting values are −17.5(5) and −17.1(5) kJ/mol for $Cr_3(btc)_2$ and $Cu_3(btc)_2$, respectively. Additional isotherm plots and details

DOI: 10.1021/jacs.5b06657
J. Am. Chem. Soc. 2015, 137, 10816−10825

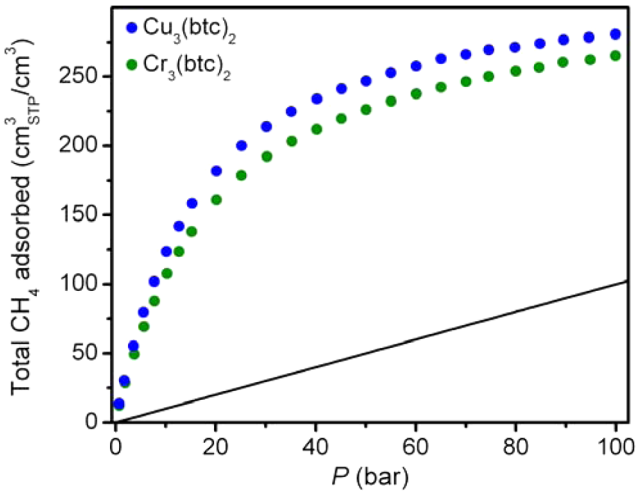

Figure 1. Comparison of the total volumetric CH_4 adsorption of $Cr_3(btc)_2$ (green) and $Cu_3(btc)_2$ (blue) at 25 °C. The solid black line corresponds to the amount of CH_4 that would be present in a tank with no adsorbent.

regarding the analysis of adsorption data are provided in the Supporting Information.

Neutron Diffraction Data. Neutron diffraction data were first collected for activated $Cr_3(btc)_2$, and its structure was refined to obtain a high quality starting model for the subsequent CD_4 dosed data. While the framework topology is nearly identical to that of $Cu_3(btc)_2$, there is a slight but important difference in the inorganic paddlewheel of $Cr_3(btc)_2$ (Figure 2). The short Cr−Cr distance of 1.949(6) Å indicates

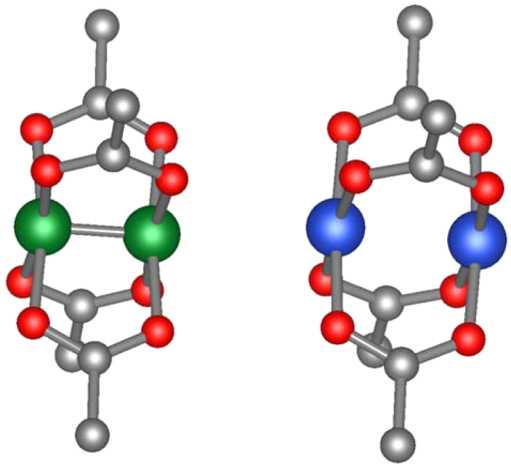

Figure 2. Paddlewheel units in $Cr_3(btc)_2$ (left) and $Cu_3(btc)_2$ (right). Green, blue, gray, and red spheres represent Cr, Cu, C, and O atoms, respectively.

the presence of a metal−metal bond of high order,[46] which pulls the Cr atom slightly below (0.155(5) Å) the plane formed by the four O atoms of the carboxylate ligands. In $Cu_3(btc)_2$, the Cu−Cu distance of 2.465(3) Å is long enough that the Cu atom lies above the plane of the four O atoms of the carboxylate ligands, projecting slightly outward into the pore. Neutron diffraction experiments of D_2 adsorption have shown that this variance in the paddlewheel unit causes different primary adsorption sites for D_2 in $Cu_3(btc)_2$ (at the metal site) and $Cr_3(btc)_2$ (at the windows to the octahedral cages).[12,25,26] There is also an increase in unit cell volume for $Cr_3(btc)_2$ to 18984.4(9) Å^3 compared to 18205.4(8) Å^3 for activated $Cu_3(btc)_2$, an important feature to note when comparing volumetric uptake values.

Two previous reports have found binding sites for CD_4 in $Cu_3(btc)_2$ using neutron diffraction. The low loading data of Getzschmann et al.[21] was reported to be too low to identify any adsorption sites, and additional data were measured at loadings so high that nearly all the pore surface contained adsorbed molecules. The authors note that some molecules were frozen at sites that are not equilibrium positions, likely due to the appreciably low temperature (77 K) at which the materials were dosed. Data from Wu et al.[22] measured at moderate loading levels identified the metal site and the windows to the octahedral cages as strong adsorption sites; however, CD_4 molecules were still found at several different sites simultaneously making it difficult to draw comparisons regarding their relative strengths. A very recent report by Zhou and coworkers[23] detailed the use of a time-resolved diffraction structure envelope (TRDSE) method applied to synchrotron X-ray diffraction data to examine dynamic effects of adsorption in $Cu_3(btc)_2$ and other similar MOFs. The neutron diffraction results presented here, correlated with isotherm data and computational results, provide insights that differ significantly from several of the conclusions drawn using that method, as we will explain in detail below.

Our procedure for neutron diffraction experiments involved dosing the evacuated material at 150 K, well above the condensation point of CH_4 (111.6 K at 1 bar). The material was then slowly cooled while monitoring the pressure drop in the system to mitigate any possibility of gas condensation in the material. Once the entire dose was adsorbed, the material was then cooled to 8 K for data collection. Structures were obtained at loadings of 0.4, 0.7, 1.5, and 2.2 CD_4 molecules per Cu atom in $Cu_3(btc)_2$, and 0.7, 1.5, and 2.2 CD_4 molecules per Cr atom in $Cr_3(btc)_2$. The Fourier difference maps generated during the refinement of the two lowest $Cu_3(btc)_2$ loadings and the lowest $Cr_3(btc)_2$ loading clearly show that the initial adsorption site is at the windows to the octahedral cages (Figure 3). It is also apparent that the D atoms are in localized positions, and there is a preferred orientation of the CD_4 molecule, with one C−D bond aligned "inward" toward the center of the octahedral cage. This window site is one crystallographically unique site repeated over the four windows for each octahedral cage, and full occupation of this site corresponds to 2/3 of a CD_4 molecule per metal atom. It is important to note that at these loadings, no residual nuclear density was evident at the open metal site in the Fourier difference maps, unequivocally showing that the window site is preferred for both materials.

With increased dosing to 1.5 CD_4 per metal atom, additional nuclear density was found inside the octahedral cages and at the metal sites in a similar fashion for both $Cu_3(btc)_2$ and $Cr_3(btc)_2$. With respect to the octahedral cage site, refinements in which a CD_4 molecule was placed at the center of the cage resulted in poor fitting to experimental data. This is not surprising since the molecule can form shorter interactions with the inside surface of the cage if it is located slightly displaced from the center of the pore (Figure 4). In this position, the C atom of the CD_4 molecule is closer to the center of the benzene rings that form the cage walls than if it were positioned in the exact center of the cage (by approximately 0.18 Å). Adsorption at this off-center location has been observed and well-modeled previously in our analysis of Kr adsorbed within $Cu_3(btc)_2$.[24]

DOI: 10.1021/jacs.5b06657
J. Am. Chem. Soc. 2015, 137, 10816−10825

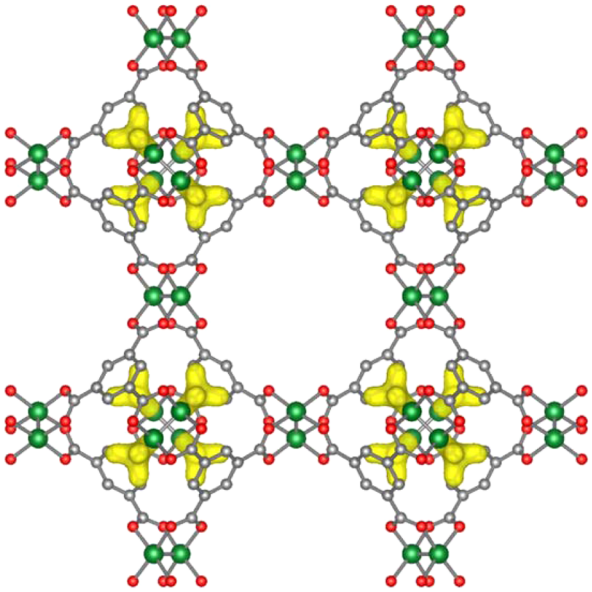

Figure 3. Real space Fourier difference nuclear scattering length density (yellow surface) generated during the initial Rietveld refinement step for the 0.7 CD_4 per Cr atom data superimposed on one unit cell of the $Cr_3(btc)_2$ structure viewed down the *a*-axis, clearly indicating the presence of adsorbed CD_4 in the windows of the octahedral cages with a specific orientation. Green, gray, and red spheres represent Cr, C, and O atoms, respectively; H atoms are omitted for clarity. Similar maps were obtained for the 0.4 and 0.7 CD_4 per Cu atom loadings in $Cu_3(btc)_2$.

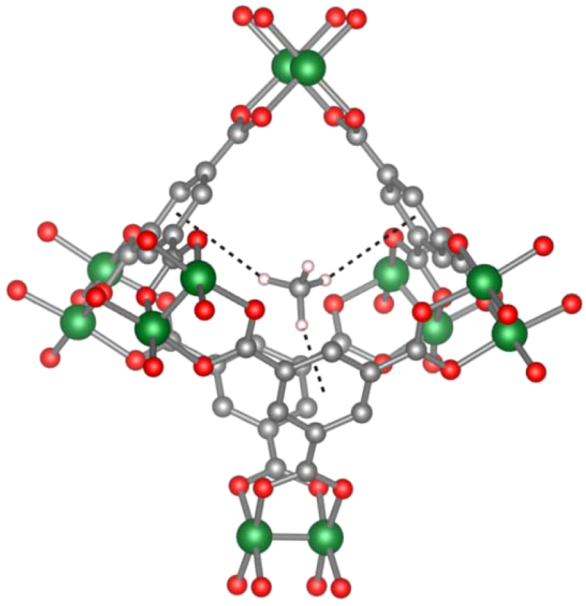

Figure 4. A CD_4 molecule adsorbed at the off-center octahedral cage site of $Cr_3(btc)_2$ in the 1.5 CD_4 per Cr atom structure. Adsorbed molecules at the window and metal sites are not shown for clarity. Only one of the four disordered and identical sites are shown. The black dashed lines indicate the close contacts between the D atoms and the center of the three benzene rings forming the cage surfaces. Green, gray, red, and light pink spheres represent Cr, C, O, and D atoms, respectively; H atoms are omitted for clarity.

Concurrent with adsorption on this site, we observe a rearrangement of the CD_4 molecules in the window sites where the molecules are now located slightly farther away from the center of the octahedral cage than in the 0.7 CD_4 per metal structures (by approximately 0.4−0.5 Å). These molecules also partially rotate in order to accommodate the additional CD_4 molecule in the octahedral cage. This is modeled in the 1.5 and 2.2 CD_4 per Cu and Cr structures by incorporating disorder between two inverted CD_4 molecules at the window site and refining their atomic parameters simultaneously. This slight movement of the adsorbed molecules is reasonable considering each successive dose is performed by heating the system to 150 K. The additional adsorption site inside the octahedral cage is an indication that CH_4−CH_4 interactions play a significant role in the adsorption mechanism, which will be examined further below.

Adsorption at the metal site is also evident in the 1.5 CD_4 per metal atom structures. Through analysis of the Fourier difference plots, it is clear that the CD_4 molecule binds at the metal site with one of the D atoms projecting outward into the center of the pore approximately 180° away from the metal atoms and the other three D atoms are disordered as a ring of scattering density above the metal sites. The previous structural report mentioned above on CD_4 in $Cu_3(btc)_2$ removed this disorder by reducing the symmetry of the structure to the $R\bar{3}$ space group, one in which three unique D atoms can be placed in the area where this ring exists.[22] Our refinements in this work proceeded most smoothly without this symmetry reduction and instead modeling the D atoms of this molecule with disorder over nine different sites to approximate the torus of scattering (more details and images of CD_4 modeling at the metal site are available in the Supporting Information).

While binding at the metal site occurs at the same position and loading levels for both $Cu_3(btc)_2$ and $Cr_3(btc)_2$, there are slight differences in the effects this has on the overall structure that are related to the differences in the nature of the paddlewheel. The metal−CD_4 distance is smaller for $Cu_3(btc)_2$ than for $Cr_3(btc)_2$ (2.847(5) Å vs 3.09(2) Å) at a loading of 1.5 CD_4 per metal, as measured from the metal atom to the C atom of the CD_4 molecule. Also, while the Cu−Cu distance remains relatively unchanged upon CD_4 binding, the Cr−Cr distance lengthens from 1.949(6) Å to 2.08(3) Å in the 1.5 CD_4 per Cr atom structure, and 2.14(1) Å in the 2.2 CD_4 per Cr atom structure. This lengthening is similar to that reported previously for D_2 adsorption and potentially indicates a decrease in the Cr−Cr bond order.[12] However, unlike in the case of D_2 binding, here the Cr does move to the point that it projects outward above the plane of the four oxygen atoms from the carboxylate ligand. While the two sites around the octahedral cage are effectively fully occupied at the 1.5 CD_4 per metal atom loadings for both materials, the refined fractional occupancies of the CD_4 molecules at the metal sites are only 0.793(4) and 0.673(9) for $Cu_3(btc)_2$ and $Cr_3(btc)_2$, respectively. This further confirms that the site inside the octahedral cage fills, and the window molecules rearrange as described above, prior to adsorption occurring at the metal site.

At the highest dose of 2.2 CD_4 per metal atom, the first three binding sites described above are fully occupied, and a fourth site begins to populate in the 11 Å diameter pore. This site is located above the outside of the ligands that form the surface of the octahedral cages and essentially represents the filling of the surface of one of the large pores (Figure 5). An additional dosing of 3.3 CD_4 per Cu atom was measured; however, significantly increased background in the diffraction patterns prevented the refinement of additional binding sites within the large pores (see the Supporting Information for data). This is

DOI: 10.1021/jacs.5b06657
J. Am. Chem. Soc. 2015, 137, 10816−10825

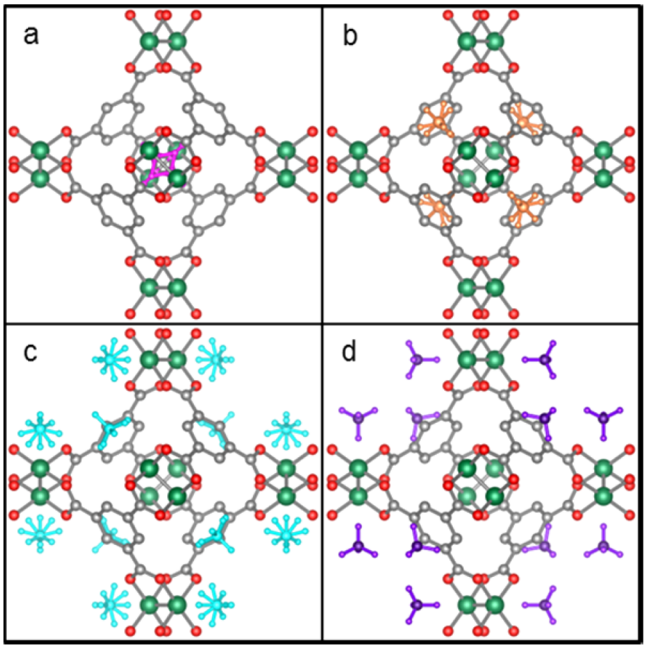

Figure 5. Structure of approximately half of the unit cell of $Cr_3(btc)_2$ dosed with 2.2 CD_4 per Cr atom viewed down the *a*-axis. Green, gray, and red spheres represent Cr, C, and O atoms, respectively; H atoms are omitted for clarity. CD_4 molecules are shown at the octahedral cage site (a, pink) the window site (b, orange), the metal site (c, cyan), and the fourth site (d, purple).

likely a result of short-range order in the additional adsorption that does not contribute significantly to the crystalline order of the previous adsorption sites, a phenomenon that has been previously observed for H_2 adsorption in nanoporous materials.[47]

While these structures indicate a sequential occupation of the four adsorption sites, they do not necessarily contradict with the adsorption data in which the isotherms are well modeled by a Langmuir equation with a single CH_4 binding site. Specifically, the energy differences between CH_4 adsorption at the strongest binding sites are likely most important at low temperatures, and the single-site Langmuir model should represent the average binding energy of CH_4 across these sites. Indeed, the dosing method used for the above diffraction measurements involved CD_4 adsorption at 150 K followed by cooling to 8 K upon complete adsorption of the gas, whereas the isotherms were measured at more relevant conditions near room temperature.

To investigate potential differences in site occupation with respect to temperature, we performed additional neutron diffraction measurements on $Cu_3(btc)_2$ at 150 and 295 K dosed with approximately 1.3 CD_4 molecules per Cu atom. We chose this value to ensure that multiple sites were occupied at 150 K, and so that we could clearly distinguish residual adsorbed gas even at 295 K. The Fourier difference map derived from the data at 150 K (Figure 6, left) clearly shows CD_4 molecules at, or close to, the three strongest sites found in the 8 K data—the octahedral cage, window, and metal sites. The quality of the data is sufficient for a full Rietveld refinement using the same model as discussed above (full details and goodness-of-fit parameters are given in the Supporting Information). The resulting CD_4 fractional occupancies indicate a more even distribution across these sites than at lower temperatures where the sites fill successively (Table 1).

Table 1. Occupancy Levels for the Three Strongest Binding Sites with Respect to Temperature As Determined through Neutron Diffraction Experiments

temperature (K)	window site occupancy	octahedral cage site occupancy	metal site occupancy
150	0.75(4)	0.428(8)	0.598(7)
295	0.092(6)	0.40(2)	none

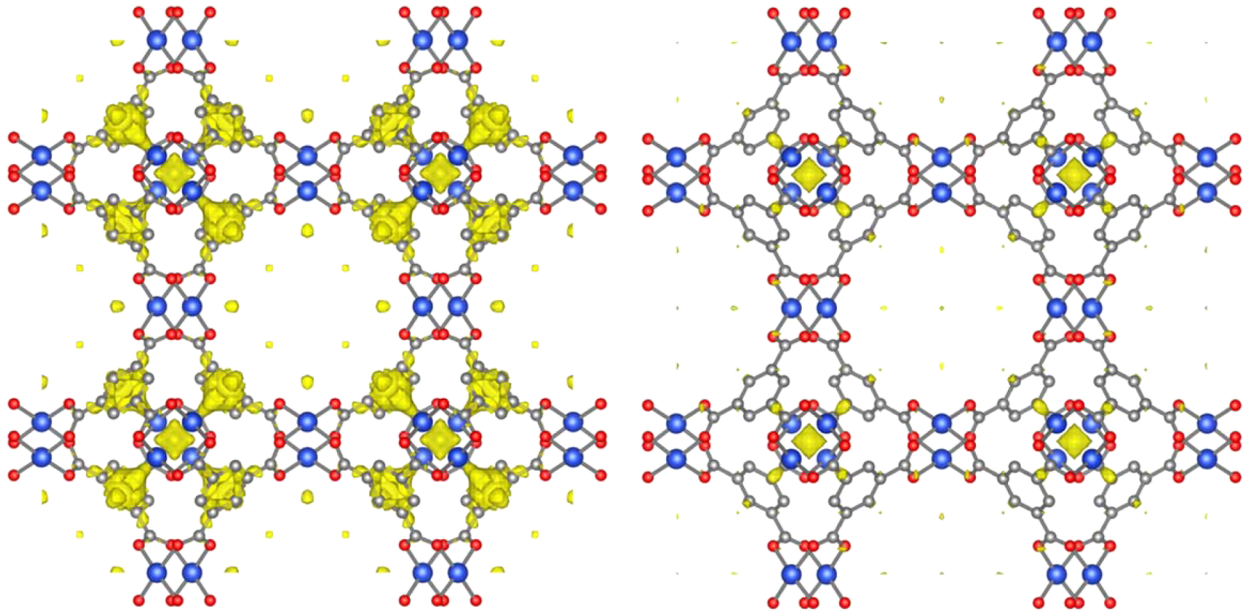

Figure 6. Real space Fourier difference nuclear scattering density (yellow surface) generated during the initial Rietveld refinement step for the 1.3 CD_4 per Cu atom data measured at 150 K (left) and 295 K (right) superimposed on one unit cell of the $Cu_3(btc)_2$ structure viewed down the *a*-axis. Blue, gray, and red spheres represent Cu, C, and O atoms, respectively; H atoms are omitted for clarity.

DOI: 10.1021/jacs.5b06657
J. Am. Chem. Soc. 2015, 137, 10816−10825

The sample was subsequently warmed to 295 K, causing most of the CD_4 to desorb and resulting in a pressure of approximately 1.7 bar in the closed system. The Fourier difference intensities (Figure 6, right) indicate the localization of CD_4, and Rietveld refinement indicates a small amount of CD_4 located both inside the octahedral cages and at the window sites, with no CD_4 at the metal sites. Total refined occupancies of these sites are low (Table 1), as expected given the isotherm data measured at room temperature and low pressures (Figure S4).

At this point it is worth noting that these results and interpretations are significantly different from those obtained using the TRDSE maps presented in the recent report by Zhou and co-workers.[23] This methodology involved the measurement of powder diffraction patterns under nonequilibrium conditions, which in itself implies the potential for variability in the number of crystallographic phases present at any given time during the measurement. In such a scenario, the actual structure of the material is constantly changing during the collection of any single powder pattern. The collected data will be composed of contributions from diffraction patterns of crystallites of different sizes and morphologies, each experiencing potentially different local temperature and chemical potentials on the nanoscale. These effects would be impossible to untangle from the data if there is little effect on the lattice constants, or more importantly, on the few Bragg peaks at low angles that are used in the data analysis. Such is the case here, and this indistinguishable summation of peak intensities likely leads to erroneous interpretations of the adsorption process. For instance, when compared to our equilibrium diffraction results where we are monitoring the average crystal structure, as well as the other previous reports of CH_4 adsorption behavior in $Cu_3(btc)_2$,[21,22] the TRDSE maps provide several unique observations that are in conflict with those derived from the other methods. Most significantly, the TRDSE maps lead to an assertion that there exists an energy barrier to adsorption at the window sites, which CH_4 molecules lack the energy to overcome at low temperatures; however, all previous experimental data actually indicate CH_4 adsorption in the octahedral cage and window sites at low temperatures. The TRDSE results also imply that CH_4 molecules are stuck behind at the metal sites upon desorption at 295 K; however, our equilibrium structure at that temperature clearly shows CH_4 inside the octahedral pocket and not at the metal site, on average. Interestingly, the GCMC simulations provided in the same TRDSE report for CH_4 adsorption at 150 K also show better correlation with all the other forms of experimental data than with the TRDSE results. Taken together, these observations indicate variability in results from the TRDSE methodology leading to inaccurate interpretation of the adsorption properties of the $Cu_3(btc)_2$ system, and raise questions about the applicability of this method to analyzing adsorption in other MOFs.

To summarize our diffraction results, while the sites in the octahedral cage are preferred over the metal sites at low temperatures, all of these can be considered moderately strong binding sites. This explains why the adsorption isotherm data at relevant temperatures are best fit using a single-site Langmuir equation. These materials contain a high concentration of strong binding sites per unit volume, resulting in high total volumetric uptake values. As the filling of adsorption sites are identical for both $Cr_3(btc)_2$ and $Cu_3(btc)_2$, and the overall strength of these interactions are similar, it can be inferred that the main reason $Cu_3(btc)_2$ has a higher volumetric uptake compared to $Cr_3(btc)_2$ is due to its slightly smaller unit cell. The major conclusions evident from the combination of the isotherm data and the diffraction data are that adsorption mechanisms are essentially identical for $Cu_3(btc)_2$ and $Cr_3(btc)_2$, and that the binding sites in and around the octahedral cage are favored over both metal sites. Since the presence of two distinct binding sites is not required to model the variable temperature adsorption isotherms, it is not immediately clear why CH_4 adsorption occurs first at the octahedral cage and window sites, rather than at the metal sites. In an effort to better understand the origins of this surprising sequential filling of adsorption sites, a detailed computational analysis was performed for CH_4 binding in $Cr_3(btc)_2$ and $Cu_3(btc)_2$.

Computational Results. Prior to studying the adsorption process itself, the electronic structure of the frameworks must be determined. The electronic configuration of copper paddlewheel systems like $Cu_3(btc)_2$ are well-established; the unit contains two d^9 Cu(II) centers with one unpaired electron localized on each metal. On the other hand, the electronic configuration of the Cr−Cr bond is far from obvious, and calculations were thus performed with a multiconfigurational method, in this case spin-flip complete active space with nondegenerate perturbative single excitations (SF-CAS(S)) calculations (presented in detail in the Supporting Information).[48,49] From these calculations on a cluster model, the ground state was determined to be a singlet with significant multireference character. The dominant configurations of the Cr−Cr bond are $\pi^2\bar{\pi}^2\delta^1\bar{\delta}^1$ (23%) and $\pi^2\bar{\pi}^2\delta^{*1}\bar{\delta}^{*1}$ (15%), yielding a bond order of approximately 3. Furthermore, our SF-CAS(S) calculations do not indicate a difference in orbital energies or electronic states whether CH_4 is adsorbed at the metal site or not. We can therefore conclude that the electronic structure of the Cr−Cr bond is not strongly affected by CH_4 adsorption at a fixed geometry.

Binding energies for CH_4 were determined by periodic DFT calculations at the window and metal sites (Table 2) and converted to binding enthalpies by applying harmonic vibrational corrections. For $Cu_3(btc)_2$ these values were determined to be −21.8 and −9.4 kJ/mol for the window and metal sites, respectively. A similar value of −21.5 kJ/mol for the window site in $Cr_3(btc)_2$ was calculated; however, since DFT is unable to access the multireference singlet ground state of the Cr−Cr

Table 2. Calculated CH_4 Binding Enthalpies in kJ/mol for a Single CH_4 Adsorbed at the Metal and Window Sites in the Respective Empty Frameworks Computed at the vdW-DF2 Level of Theory[a]

structure	metal site (kJ/mol)	window site (kJ/mol)	experimental (kJ/mol)
$Cu_3(btc)_2$	−9.4	−21.8	−17.1
$Cu_3(btcBr_3)_2$	−15.0	−23.9	
$Cu_3(btcMe_3)_2$	−13.7	−25.1	
$Cr_3(btc)_2$	[b]	−21.5	−17.5
$Cr_3(btcBr_3)_2$	[b]	−23.0	
$Cr_3(btcMe_3)_2$	[b]	−23.3	

[a]Experimental values determined above for $Cu_3(btc)_2$ and $Cr_3(btc)_2$ are included for comparison. [b]Binding at the Cr metal−metal bond is very sensitive to the presence of a guest and requires proper description of the electronic structure of the bond; therefore, binding energies at the DFT level are not included.

DOI: 10.1021/jacs.5b06657
J. Am. Chem. Soc. 2015, 137, 10816−10825

bond, accurate estimations of binding enthalpies at the metal site are unreliable at the DFT level of theory and are not included. Since the adsorption data are nearly identical for the two materials, in this section we will focus our discussion on $Cu_3(btc)_2$. The calculations at the DFT level are representative of an infinite dilution of CH_4, and the calculated difference in energy between the window and metal sites is consistent with the observation in our NPD results that the window sites are occupied first.

To investigate the consequences of these two different binding energies, and draw a comparison with the measured and calculated adsorption isotherms where more than one CH_4 molecule is present, we hypothesized that the strength of CH_4 binding at the Cu^{2+} sites might be effectively increased by intermolecular interactions with CH_4 molecules already adsorbed at the nearby window sites.[50] The effect of lateral CH_4−CH_4 interactions has been shown by other researchers to be important and, given that CH_4−CH_4 distances are quite short in this topology, we suspected they may play an important role here. It should be noted that in the $Cu_3(btc)_2$ topology, the window and metal binding sites are separated by close to the ideal CH_4−CH_4 distance of 4.2 Å, based on our LJ potential.[44,51] With this in mind, we recomputed the binding energy at the metal site in order to decompose the interactions between the CH_4 molecules and the framework by considering their effects stepwise. Our first approach was at infinite dilution (CH_4 interacting with the framework only at the metal site). Next, one CH_4 was fixed at its minimum energy geometry in the window site, and the binding of a second CH_4 at the metal site was computed. The presence of one CH_4 alone increases the binding strength by −1.28 kJ/mol. However, if the structures of both CH_4 molecules are allowed to relax, as opposed to only the CH_4 in the metal site, binding at the metal site increases further leading to an enhancement of −5.49 kJ/mol (or −2.74 kJ/mol per CH_4). Furthermore, at the configuration from NPD with the highest loading, the CH_4 at the metal site interacts with not one but eight CH_4 molecules. Specifically, there are two neighboring window sites at a distance of 4.36 Å, four neighboring metal sites at a distance of 5.17 Å, and two additional CH_4 molecules at a distance of 6.39 Å.

Using the TrAPPE force field, a single CH_4−CH_4 interaction at the shortest distance of 4.36 Å is −1.67 kJ/mol, for example. In the experimental geometry, the sum of all pairwise TrAPPE CH_4−CH_4 interactions suggest an enhancement of binding by ∼5 kJ/mol at the metal site. We note that while the absolute value of this energy should be thought of as a rough approximation, this result emphasizes the importance of the cumulative effect of interactions between neighboring CH_4 molecules. Due to these interactions, the effective binding energy at the metal site is not that different from the binding energy at the window site, further explaining why a dual-site Langmuir isotherm was not necessary to fit the data. Simply accounting for these additional interactions can connect the conclusions drawn from the experimental data. Since the nature of the metal cation imparts very little effect on the adsorption mechanism and the strong binding is due to a combination of structural features that are identical in both materials as well as CH_4−CH_4 interactions, uptake values for $Cu_3(btc)_2$ and $Cr_3(btc)_2$ are similar.

With the underlying adsorption mechanisms well-understood, we turned our attention to the simulation of volumetric uptake. Total volumetric CH_4 adsorption isotherms computed with grand canonical Monte Carlo (GCMC) using the UFF-shifted force field describe the experimental isotherms presented above very well (Figure 7). Given this good

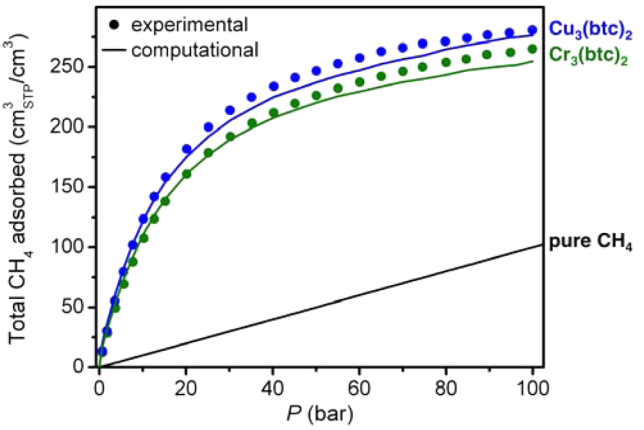

Figure 7. Experimental and calculated isotherms of total volumetric uptake for $Cu_3(btc)_2$ (blue) and $Cr_3(btc)_2$ (green). Experimental results are shown as circles, and the shifted-UFF isotherm as solid lines.

agreement, we extended these calculations to evaluate CH_4 adsorption in some structural variations of $Cu_3(btc)_2$ and $Cr_3(btc)_2$ and to gain insight into the possibility of developing an improved adsorbent. As the identity of the metal cation seems somewhat unimportant, these variations involved hypothetical substituted versions of the btc^{3-} ligand. Both Cu and Cr structures with the tribromo- and trimethyl- substituted ligand molecules, denoted $btcBr_3^{3-}$ and $btcMe_3^{3-}$ (Figure 8),

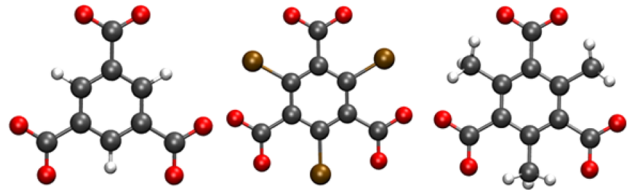

Figure 8. Three ligands used for simulations, btc^{3-} (left), $btcBr_3^{3-}$ (center), and $btcMe_3^{3-}$ (right). Gray, red, white, and brown spheres represent C, O, H, and Br atoms, respectively.

were investigated. Our objective was to investigate if larger substituents projecting into the window sites and a different electronic structure at the metal sites would result in stronger CH_4 adsorption and higher volumetric CH_4 uptake. Calculated binding energies indicate that ligand functionalization does result in an increase in binding enthalpies at both the window and metal sites for both the Cu and Cr analogues (Table 2). It is more relevant, however, to examine the resulting volumetric capacities determined from the simulated isotherms in these materials. The deliverable capacity, typically evaluated for adsorption at 35 bar and desorption at 5.8 bar, is an even more important metric. Table 3 shows the deliverable capacities obtained from the difference between UFF/TraPPE volumetric uptake values at various industrially relevant pressures. While binding enthalpies are increased by ligand substitution, deliverable capacity decreases in all cases from the non-functionalized materials.

If ligand substitution does not result in improved performance, we can try to optimize further our best performing

DOI: 10.1021/jacs.5b06657
J. Am. Chem. Soc. 2015, 137, 10816−10825

Table 3. Total and Deliverable Capacities Obtained from Simulated UFF/TraPPE Isotherms for the Various Structures for 35 Bar Adsorption and 5.8 Bar Desorption

framework	35 bar total capacity (cm^3/cm^3)	35 bar deliverable capacity (cm^3/cm^3)
$Cu_3(btc)_2$	173	114
$Cu_3(btcBr_3)_2$	154	75
$Cu_3(btcMe_3)_2$	196	96
$Cr_3(btc)_2$	179	121
$Cr_3(btcBr_3)_2$	155	79
$Cr_3(btcMe_3)_2$	201	104

material. For example, suppose we can tune the binding energy to determine whether this would lead to a better performing structure. Computationally, we can do this directly using the method of Kim et al. by shifting the force field to target our binding energy and computing the corresponding heat of adsorption and deliverable capacity. Figure 9 shows that even if

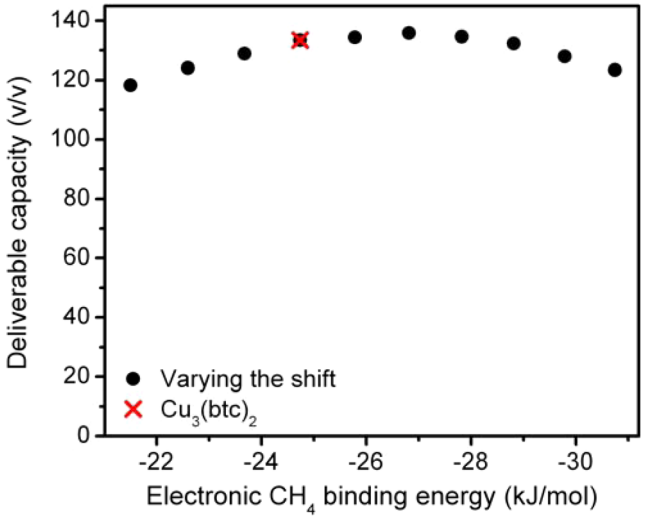

Figure 9. Heat of adsorption used as the shift in order to calculate the adsorption isotherm was varied to determine what value would lead to the largest 35 bar deliverable capacity. The calculated result for $Cu_3(btc)_2$ using the same level of theory is included for comparison (red x).

we would have the possibility to increase or decrease the heat of adsorption as much as 6 kJ/mol, there is no significant increase in the deliverable capacity beyond what is calculated for the actual $Cu_3(btc)_2$ structure. This demonstrates that the $Cu_3(btc)_2$ structure already provides nearly the highest deliverable capacity that could be achieved even if the energetics of this structure-type could be altered.

In a recent computational screening of over 650 000 materials, $Cu_3(btc)_2$ was shown to be among the highest performing for CH_4 storage.[32] When designing a material for CH_4 storage, the framework−CH_4 interaction energies, the number of binding sites, and the CH_4−CH_4 interactions all play an important role.[30] In this particular case, we have varied the energetic contributions and have shown that $Cu_3(btc)_2$ already has the ideal binding enthalpy required to maximize the deliverable capacity. With a higher heat of adsorption, the deliverable capacity is lowered because the increase in loading at low pressures is larger than the increase in loading at high pressures. Decreasing the binding enthalpy reduces loading at high pressures to the point where the deliverable capacity also decreases.

CONCLUSIONS

To date, $Cu_3(btc)_2$ has shown the most promise of any MOF as a CH_4 storage material for relevant industrial applications. In this report, we have carried out a thorough investigation regarding the underlying mechanistic reasons for its high volumetric uptake, combining several types of experimental and computational data. The fact that enhancement of CH_4 binding at its open metal site is mostly due to CH_4−CH_4 interactions between adjacent adsorbed molecules is a very important conclusion that should assist future research into new materials for this application. Alteration of the $Cu_3(btc)_2$ structure, either by substitution of the Cu with Cr, hypothetical ligand substitutions, or using theoretical tools to vary the binding strength, does not improve the most important CH_4 uptake metrics for practical use. The structure of $Cu_3(btc)_2$ has just the right combination of features to maximize both CH_4−framework and CH_4−CH_4 interactions. Furthermore, this work highlights the level of mechanistic understanding that can be achieved when experimental and computational techniques are combined. This approach is currently being expanded to other adsorption applications in other MOF systems.

ASSOCIATED CONTENT

Supporting Information

The Supporting Information is available free of charge on the ACS Publications website at DOI: 10.1021/jacs.5b06657.

Synthetic details, additional adsorption isotherm data and details of isotherm fitting, full crystal structure details and Rietveld refinement plots, additional details of CH_4 site disorder, Cr−Cr paddlewheel calculation information, and additional simulation data for deliverable capacities at 65 bar. (PDF)

AUTHOR INFORMATION

Corresponding Authors

*zeric.hulvey@nist.gov
*craig.brown@nist.gov

Notes

The authors declare no competing financial interest.

ACKNOWLEDGMENTS

We thank Prof. Efrain Rodriguez for assistance with the synthesis of $Cr_3(btc)_2$ and Dr. Matthew Hudson for assistance with neutron powder diffraction experiments. Gas adsorption measurements were supported by the Nanoporous Materials Genome Center, which is funded by the U.S. Department of Energy, Office of Basic Energy Sciences, Division of Chemical Sciences, Geosciences, and Biosciences under Award DE-FG02-12ER16362. Computational efforts were supported by the Center for Gas Separations Relevant to Clean Energy Technologies, an Energy Frontier Research Center, funded by the U.S. Department of Energy, Office of Science, Office of Basic Energy Sciences, under Award DE-SC0001015. T.P.D. was supported through the NIST/NSF REU Summer Undergraduate Research Fellowship (SURF) funded through the Center for High Resolution Neutron Scattering (CHRNS) DMR-0944772. This research used resources of the National Energy Research Scientific Computing Center, a DOE Office of

DOI: 10.1021/jacs.5b06657
J. Am. Chem. Soc. 2015, 137, 10816−10825

Science User Facility supported by the Office of Science of the U.S. Department of Energy under Contract No. DE-AC02-05CH11231.

REFERENCES

(1) U.S. Department of Energy, Energy Information Administration, 2013, http://www.eia.gov/tools/faqs/faq.cfm?id=73&t=11, accessed 7/2/2015.
(2) U.S. E.P.A., 2013, http://www.epa.gov/climatechange/Downloads/ghgemissions/US-GHG-Inventory-2013-ES.pdf, accessed 7/2/2015.
(3) *Report: A Full Fuel-Cycle Analysis of Energy and Emissions Impacts of Transportation Fuels Produced from Natural Gas*; U.S. Dept. of Energy−Argonne National Laboratory: Argonne, IL, 1999.
(4) MIT, 2011, http://mitei.mit.edu/publications/reports-studies/future-natural-gas, accessed 7/2/2015.
(5) Makal, T. A.; Li, J.-R.; Lu, W.; Zhou, H.-C. *Chem. Soc. Rev.* **2012**, *41*, 7761−7779.
(6) Konstas, K.; Osl, T.; Yang, Y.; Batten, M.; Burke, N.; Hill, A. J.; Hill, M. R. *J. Mater. Chem.* **2012**, *22*, 16698−16708.
(7) Mason, J. A.; Veenstra, M.; Long, J. R. *Chem. Sci.* **2014**, *5*, 32−51.
(8) Peng, Y.; Krungleviciute, V.; Eryazici, I.; Hupp, J. T.; Farha, O. K.; Yildirim, T. *J. Am. Chem. Soc.* **2013**, *135*, 11887−11894.
(9) He, Y.; Zhou, W.; Qian, G.; Chen, B. *Chem. Soc. Rev.* **2014**, *43*, 5657−5678.
(10) Chui, S. S. Y.; Lo, S. M. F.; Charmant, J. P. H.; Orpen, A. G.; Williams, I. D. *Science* **1999**, *283*, 1148−1150.
(11) Murray, L. J.; Dincă, M.; Yano, J.; Chavan, S.; Bordiga, S.; Brown, C. M.; Long, J. R. *J. Am. Chem. Soc.* **2010**, *132*, 7856−7857.
(12) Sumida, K.; Her, J.-H.; Dinca, M.; Murray, L. J.; Schloss, J. M.; Pierce, C. J.; Thompson, B. A.; FitzGerald, S. A.; Brown, C. M.; Long, J. R. *J. Phys. Chem. C* **2011**, *115*, 8414−8421.
(13) Wade, C. R.; Dincă, M. *Dalton Trans.* **2012**, *41*, 7931−7938.
(14) Dincă, M.; Dailly, A.; Brown, C. M.; Neumann, D. A.; Long, J. R. *J. Am. Chem. Soc.* **2006**, *128*, 16876−16883.
(15) Wu, H.; Zhou, W.; Yildirim, T. *J. Am. Chem. Soc.* **2009**, *131*, 4995−5000.
(16) Wu, H.; Zhou, W.; Yildirim, T. *J. Phys. Chem. C* **2009**, *113*, 3029−3035.
(17) Bloch, E. D.; Queen, W. L.; Krishna, R.; Zadrozny, J. M.; Brown, C. M.; Long, J. R. *Science* **2012**, *335*, 1606−1610.
(18) Herm, Z. R.; Wiers, B. M.; Mason, J. A.; van Baten, J. M.; Hudson, M. R.; Zajdel, P.; Brown, C. M.; Masciocchi, N.; Krishna, R.; Long, J. R. *Science* **2013**, *340*, 960−964.
(19) Lee, K.; Isley, W. C.; Dzubak, A. L.; Verma, P.; Stoneburner, S. J.; Lin, L.-C.; Howe, J. D.; Bloch, E. D.; Reed, D. A.; Hudson, M. R.; Brown, C. M.; Long, J. R.; Neaton, J. B.; Smit, B.; Cramer, C. J.; Truhlar, D. G.; Gagliardi, L. *J. Am. Chem. Soc.* **2014**, *136*, 698−704.
(20) Queen, W. L.; Hudson, M. R.; Bloch, E. D.; Mason, J. A.; Gonzalez, M. I.; Lee, J. S.; Gygi, D.; Howe, J. D.; Lee, K.; Darwish, T. A.; James, M.; Peterson, V. K.; Teat, S. J.; Smit, B.; Neaton, J. B.; Long, J. R.; Brown, C. M. *Chem. Sci.* **2014**, *5*, 4569−4581.
(21) Getzschmann, J.; Senkovska, I.; Wallacher, D.; Tovar, M.; Fairen-Jimenez, D.; Duren, T.; van Baten, J. M.; Krishna, R.; Kaskel, S. *Microporous Mesoporous Mater.* **2010**, *136*, 50−58.
(22) Wu, H.; Simmons, J. M.; Liu, Y.; Brown, C. M.; Wang, X.-S.; Ma, S.; Peterson, V. K.; Southon, P. D.; Kepert, C. J.; Zhou, H.-C.; Yildirim, T.; Zhou, W. *Chem. - Eur. J.* **2010**, *16*, 5205−5214.
(23) Chen, Y.-P.; Liu, Y.; Liu, D.; Bosch, M.; Zhou, H.-C. *J. Am. Chem. Soc.* **2015**, *137*, 2919−2930.
(24) Hulvey, Z.; Lawler, K. V.; Qiao, Z.; Zhou, J.; Fairen-Jimenez, D.; Snurr, R. Q.; Ushakov, S. V.; Navrostky, A.; Brown, C. M.; Forster, P. M. *J. Phys. Chem. C* **2013**, *117*, 20116−20126.
(25) Peterson, V. K.; Liu, Y.; Brown, C. M.; Kepert, C. J. *J. Am. Chem. Soc.* **2006**, *128*, 15578−15579.
(26) Peterson, V. K.; Brown, C. M.; Liu, Y.; Kepert, C. J. *J. Phys. Chem. C* **2011**, *115*, 8851−8857.
(27) Wilmer, C. E.; Leaf, M.; Lee, C. Y.; Farha, O. K.; Hauser, B. G.; Hupp, J. T.; Snurr, R. Q. *Nat. Chem.* **2012**, *4*, 83−89.
(28) Sikora, B. J.; Wilmer, C. E.; Greenfield, M. L.; Snurr, R. Q. *Chem. Sci.* **2012**, *3*, 2217−2223.
(29) Wilmer, C. E.; Farha, O. K.; Bae, Y.-S.; Hupp, J. T.; Snurr, R. Q. *Energy Environ. Sci.* **2012**, *5*, 9849−9856.
(30) Simon, C. M.; Kim, J.; Lin, L.-C.; Martin, R. L.; Haranczyk, M.; Smit, B. *Phys. Chem. Chem. Phys.* **2014**, *16*, 5499−5513.
(31) Gómez-Gualdrón, D. A.; Wilmer, C. E.; Farha, O. K.; Hupp, J. T.; Snurr, R. Q. *J. Phys. Chem. C* **2014**, *118*, 6941−6951.
(32) Simon, C. M.; Kim, J.; Gómez-Gualdrón, D. A.; Camp, J. S.; Chung, Y. G.; Martin, R. L.; Mercado, R.; Deem, M. W.; Gunter, D.; Haranczyk, M.; Sholl, D. S.; Snurr, R. Q.; Smit, B. *Energy Environ. Sci.* **2015**, *8*, 1190.
(33) Rowsell, J. L. C.; Yaghi, O. M. *J. Am. Chem. Soc.* **2006**, *128*, 1304−1315.
(34) Larson, A. C.; VonDreele, R. B. *General Structure Analysis System (GSAS)*; Los Alamos National Laboratory: Los Alamos, NM, 2000; Report LAUR 86−748.
(35) Toby, B. H. *J. Appl. Crystallogr.* **2001**, *34*, 210−213.
(36) Momma, K.; Izumi, F. *J. Appl. Crystallogr.* **2011**, *44*, 1272−1276.
(37) Kresse, G.; Furthmüller, J. *Phys. Rev. B: Condens. Matter Mater. Phys.* **1996**, *54*, 11169−11186.
(38) Dion, M.; Rydberg, H.; Schröder, E.; Langreth, D. C.; Lundqvist, B. I. *Phys. Rev. Lett.* **2004**, *92*, 246401.
(39) Lee, K.; Murray, E. D.; Kong, L.; Lundqvist, B. I.; Langreth, D. C. *Phys. Rev. B: Condens. Matter Mater. Phys.* **2010**, *82*, 081101.
(40) Liechtenstein, A. I.; Anisimov, V. I.; Zaanen, J. *Phys. Rev. B: Condens. Matter Mater. Phys.* **1995**, *52*, R5467−R5470.
(41) Wang, L.; Maxisch, T.; Ceder, G. *Phys. Rev. B: Condens. Matter Mater. Phys.* **2006**, *73*, 195107.
(42) Blöchl, P. E. *Phys. Rev. B: Condens. Matter Mater. Phys.* **1994**, *50*, 17953−17979.
(43) Rappe, A. K.; Casewit, C. J.; Colwell, K. S.; Goddard, W. A., III; Skiff, W. M. *J. Am. Chem. Soc.* **1992**, *114*, 10024−10035.
(44) Kim, J.; Lin, L.-C.; Lee, K.; Neaton, J. B.; Smit, B. *J. Phys. Chem. C* **2014**, *118*, 2693−2701.
(45) Martin, M. G.; Siepmann, J. I. *J. Phys. Chem. B* **1998**, *102*, 2569−2577.
(46) Cotton, F. A.; Hillard, E. A.; Murillo, C. A.; Zhou, H.-C. *J. Am. Chem. Soc.* **2000**, *122*, 416−417.
(47) Lee, H.; Choi, Y. N.; Choi, S. B.; Kim, J.; Kim, D.; Jung, D. H.; Park, Y. S.; Yoon, K. B. *J. Phys. Chem. C* **2013**, *117*, 3177−3184.
(48) Mayhall, N. J.; Head-Gordon, M. *J. Chem. Phys.* **2014**, *141*, 044112.
(49) Mayhall, N. J.; Goldey, M.; Head-Gordon, M. *J. Chem. Theory Comput.* **2014**, *10*, 589−599.
(50) Sillar, K.; Sauer, J. *J. Am. Chem. Soc.* **2012**, *134*, 18354−18365.
(51) Martin, R. L.; Simon, C. M.; Smit, B.; Haranczyk, M. *J. Am. Chem. Soc.* **2014**, *136*, 5006−5022.

DOI: 10.1021/jacs.5b06657
J. Am. Chem. Soc. 2015, 137, 10816−10825